EARTH SURFACE PROCESSES AND LANDFORMS
Earth Surf. Process. Landforms **45**, 3055–3068 (2020)

Published online 28 July 2020 in Wiley Online Library
(wileyonlinelibrary.com) DOI: 10.1002/esp.4951

Effect of offshore waves and vegetation on the sediment budget in the Virginia Coast Reserve (VA)

William Nardin,[1]* Sara Lera[1,2] and Jaap Nienhuis[3]
[1] Horn Point Laboratory, University of Maryland Center for Environmental Science, Cambridge, MD USA
[2] Department of Civil, Constructional and Environmental Engineering, University of Rome 'La Sapienza', Rome Italy
[3] Department of Physical Geography, Utrecht University, Utrecht, NL

Received 31 March 2018; Revised 23 June 2020; Accepted 29 June 2020

*Correspondence to: William Nardin, Horn Point Laboratory, University of Maryland Center for Environmental Science, 2020 Horns Point Road, Cambridge, MD 21613, USA. E-mail: wnardin@umces.edu

ESPL
Earth Surface Processes and Landforms

ABSTRACT: The potential for rapid coastline modification in the face of sea-level rise or other stressors is alarming, since coasts are often densely populated and support valuable infrastructure. In addition to coastal submergence, nutrient-related water pollution is a growing concern for coastal wetlands. Previous studies found that the Suspended Sediment Concentration (SSC) of coastal wetlands acts as a first-order control of their sustainability, but SSC dynamics are poorly understood. Our study focuses on the Virginia Coast Reserve (VCR) Long Term Ecological Research (LTER) site, a shallow multiple tidal inlet system in the USA. We apply numerical modelling (Delft3D-SWAN) and subsequent analyses to determine SSC dynamics within the VCR. In particular, we consider two important controls on SSC in the system: vegetation (seagrass and salt marsh) and offshore waves. Our results show that vegetation colonies and increased wave energy lengthen water residence time. The reduction in the tidal prism decreases SSC export from the bay via tidal inlets, leading to increased sediment retention in the bay. We found that alongshore currents can enhance lagoon SSC by importing fine sediments from an adjacent inlet along the coastline. Our numerical experiments on vegetation seasonality can improve the understanding of wave climate impact on coastal bay sediment budget. Offshore waves increase sediment export from coastal bays, particularly during winter seasons with low vegetation density. Therefore, our study can help managers and stakeholders to understand how to implement restoration strategies for the VCR. © 2020 John Wiley & Sons, Ltd.

KEYWORDS: numerical modelling; coastal morphodynamics; sediment transport; Virginia Coast Reserve; ecogeomorphology; submerged aquatic vegetation; salt marsh

Introduction

Barrier islands and back-barrier lagoons are dynamic systems. The prospect of coastal change due to sea-level rise or other stressors is worrying because these areas are frequently densely populated and support residential and commercial infrastructures, as well as social and economic activity. Additionally, barrier islands play an influential role in the protection of land masses from forces such as flooding and storm surges.

Barrier islands are often bounded by tidal inlets. Multiple tidal inlet systems are a special case of inlet bay systems in which more than one inlet connects a single barrier lagoon with the ocean, allowing sediment and nutrient exchange, and interaction between inlets. This system exists in different types of environment but generally occurs in locations characterized by micro- and meso-tidal coasts having medium wave energy (Hayes, 1979) and back-barrier bays elongated parallel to the shoreline. Some examples are found along the Atlantic and Gulf coast of the United States (e.g. Cape Cod, Cape Hatteras, Outer Banks, Virginia barrier islands), in Mexico (Laguna de Chacahua, Laguna Madre), in the south coast of Brazil (Lagoa de Patos) and in Europe (Ria Formosa, Wadden Sea).

The flow through tidal inlets is mainly driven by tidal oscillation, flooding and draining the bay periodically, with an intensity depending on the tide and the physical characteristics of the environment (inlet geometry and planform, bay dimension and complexity) (Bruun, 1978; Aubrey and Speer, 1984). In turn, tidal flows and bay properties affect inlet geometry (O'Brien, 1969; Escoffier, 1977), which can generate morphodynamic interactions between inlets (van de Kreeke, 1990; Friedrichs *et al*, 1993; Nienhuis and Lorenzo-Trueba, 2019).

In this study, we focus on the coastal bays of the Virginia Coast Reserve (VCR). The VCR is a coastal system of microtidal shallow coastal bays (tidal range ~1.2 m) in the Delmarva Peninsula (Figure 1), with shallow seagrass beds (*Zostera marina*) and extensive fringing salt marshes (*Spartina alterniflora*). This study focuses on the hydrodynamics of this multiple tidal inlet system, and the analysis of the suspended sediment exchange between back-barrier bays and ocean, considering the effect produced by the vegetation.

The depletion of vegetated areas plays an important role in initiating or aggravating coastal flooding and poor water quality, resulting in large economic costs. In particular, loss of marsh vegetation exposes coastal communities to an increased

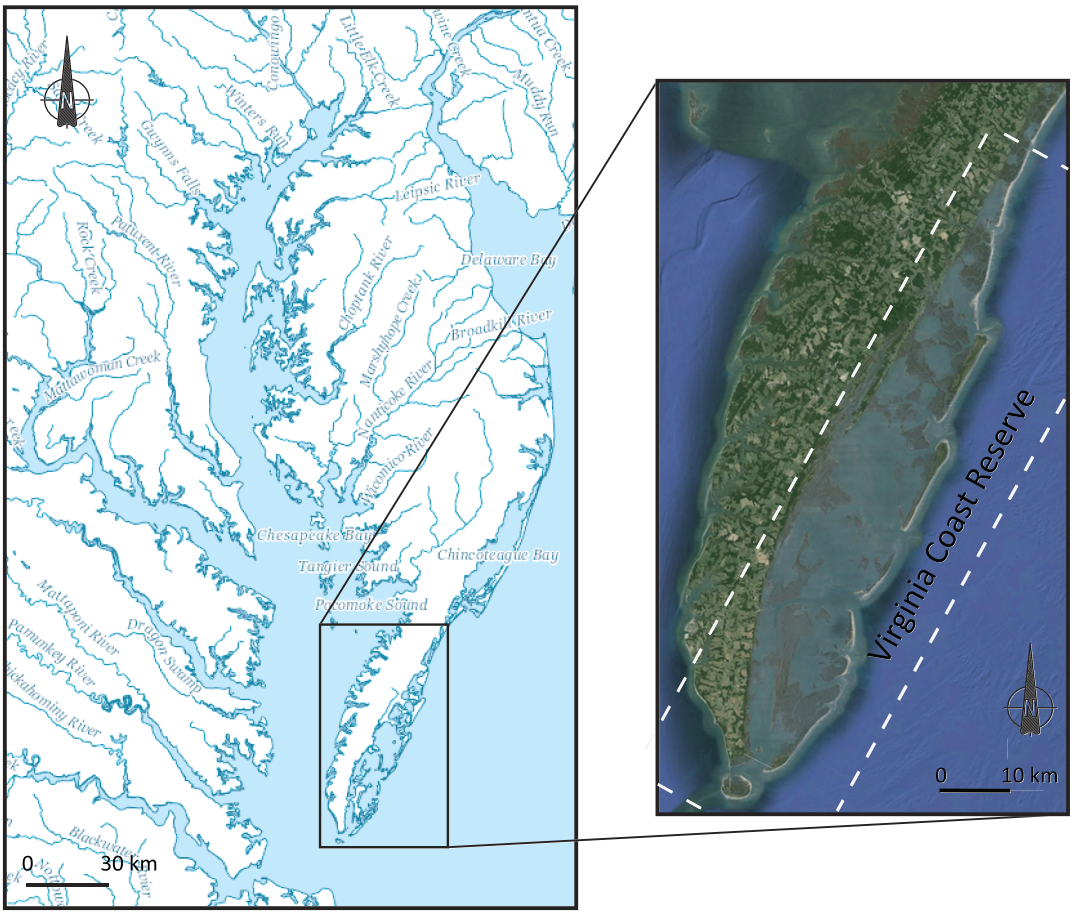

Figure 1. The study site is Virginia Coast Reserve (VA), located on the Delmarva Peninsula in the US Mid-Atlantic coast (map from US Geological Survey – National Hydrography Dataset). White dashed lines show the numerical model domain and the location of the VCR bays. (Aerial photographs courtesy of Google Earth, 2015.) [Colour figure can be viewed at wileyonlinelibrary.com]

risk of potential damage from rising sea levels. Loss of seagrasses, due to pollution or turbidity, affects coastal fisheries (Kemp *et al*, 2005; Boesch, 2006).

Coastal bays are therefore sometimes considered to be in a delicate equilibrium between vegetation and tidal inlet processes, because vegetation has a significant impact on the tidal prism and sediment balance (Stive *et al*, 1998). Vegetation serves a crucial function in trapping sediment, reducing erosion in coastal zones, and providing protection from waves during storms (Loder *et al*, 2009; Temmerman *et al*, 2013). In particular, salt marsh resistance to wave impact is intricately connected to wave dissipation over salt marsh surfaces (Duarte *et al*, 2019). During storms, coastal wetlands dissipate wave energy, reducing shore and bay bottom erosion (Moeller *et al*, 1996). Möller *et al* (2014) showed that the presence of salt marsh vegetation causes considerable wave attenuation.

At low stem density (about 100 stems m^{-2}), the drag locally enhances turbulence, causing increased shear stress and potential scour of the bed (Nepf, 1999; Bouma *et al*, 2009). However, under stem density characteristics of a typical marsh canopy (about 200 stems per m^{-2}), vegetation reduces turbulence, slows water velocity, and diminishes shear stress near the bed (Leonard and Luther, 1995; Nepf, 1999).

Vegetation produces multiscale interactions with flow and sediment transport (Fagherazzi *et al*, 2004, 2013; Moore, 2004; Larsen and Harvey, 2010; Nardin and Edmonds, 2014; Lera *et al*, 2019). Models have supplied quantitative approaches to vegetation–sediment feedback related to emergent marsh vegetation (Temmerman *et al*, 2005; Nardin *et al*, 2016) or seagrasses (Newell and Koch, 2004; Carr *et al*, 2010; Folmer *et al*, 2012).

Waves, tides and vegetation govern water fluxes and redistribution of sediments in coastal wetlands, such as the intertidal marshes and tidal flats of the VCR (Cucco and Umgiesser, 2006; Lawson *et al*, 2007; McLoughlin *et al*, 2015). A two-dimensional depth averaged (2D-H) hydro-morphodynamic model that accounts for flow fields and sediment transport is necessary to accurately estimate water fluxes and sediment concentration. We use the hydrodynamic model Delft3D (Lesser *et al*, 2004) coupled with the wave model SWAN (Booij *et al*, 1999) to determine the distribution of tidal currents and waves within the VCR bays. We focus on suspended sediment dynamics, but our study is limited to the hydrodynamics to reduce the computational time and effort. We use modern bathymetry to analyse the response of sediment transport pathways to different vegetation and offshore wave conditions. Using numerical modelling investigation, seagrass and emergent marsh grasses are specified with different sets of parameters in the Baptist (2005) vegetation schematization.

Our work extends beyond other 2D modelling studies of this area, which focused only on hydrodynamics or sediment resuspension in the bays in the absence of vegetation (Fugate *et al*, 2006; Lawson *et al*, 2007; Mariotti *et al*, 2010; Safak *et al*, 2015; Wiberg *et al*, 2015). Other studies investigate only the interaction between barrier islands and back-barrier vegetation in specific parts of the bay (Oertel, 2001; Walters *et al*, 2014; Mariotti and Canestrelli, 2017), rather than the whole system. Changes in the hydrodynamics of the inlets can modify the sediment transport patterns, increasing or decreasing the sediment supply to the downdrift zones, and, for instance, exporting from the bays suspended sediment through tidal inlets.

Outside coastal bays, alongshore currents generated by offshore waves can redistribute sediment along the coast. In particular, along a barrier island system with multiple inlets, fine sediments can exit and re-enter bays through neighbouring tidal inlets, altering their sediment budget. Previous studies focused on hydrodynamics and morphology inside the bay (Safak and Wiberg, 2012; Safak *et al*, 2015; Wiberg *et al*, 2015) or outside tidal inlets (Nienhuis and Ashton, 2016), but they miss a quantification of the whole system. Our goal is to enhance the understanding of a combination of internal bay processes and offshore wave action to include the lagoon, inlet, and nearshore coastal ocean as a whole.

Nardin *et al* (2018) investigated the independent and synergistic effects of salt marsh and seagrass in the VCR, demonstrating that vegetation promotes bay resilience; in particular, seagrass helps the salt marsh survive by reducing wave energy. It also generates more friction in subtidal zones of the bay where salt marsh cannot survive, trapping more sediment (Nardin *et al*, 2018). The study by Nardin *et al* (2018) focused inside the VCR bays, neglecting the external influence of the offshore waves.

This study aims to analyse the effect of the interaction between tidal currents, wind waves, offshore waves and vegetation on the suspended sediment concentration (SSC) patterns in the VCR. Another goal of our investigation is to quantify the processes driving the suspended sediment exchange through tidal inlets with the ocean.

Methods and Model Setup

Study area – the Virginia Coast Reserve

The VCR is a system of barrier islands, shallow bays, and salt marshes located on the southern part of the Delmarva Peninsula, along the US mid-Atlantic coast (Figure 1). The bays of the VCR, like many others on the eastern US seaboard, lack a significant fluvial source of freshwater and sediments. Shallow flats dominate the bays, with depths averaging 1 m below mean sea level. A network of tidal channels (5 m deep on average but exceeding 10 m at the inlets) connects the bays to the Atlantic Ocean. Emergent salt marsh cordgrass (*S. alterniflora*) forms fringing low marshes around the bays, while submerged eelgrass (*Z. marina*) occupies a portion of the subtidal areas shallower than a mean depth of 1.6 m. Because the study site has experienced little direct human impact, it is an ideal natural laboratory to study bay morphodynamics and salt marsh processes (McGlathery *et al*, 2007).

Collectively, wind waves, storm-induced currents, and tides constitute major controls on the spatial distribution of suspended sediment within the bays (Lawson *et al*, 2007; Wiberg *et al*, 2015). The tide in the VCR is semidiurnal, with a mean tidal range of about 1.2 m. Winds are a dominant forcing on circulation (Wiberg *et al*, 2015), with an annual average direction from the SSW and episodic northeasterly storms. The hydrodynamics of the tidal inlets are affected by the internal hydraulic connections between bays, because water in the bays of the VCR typically has access to more than one inlet. Channel configuration, hypsometry, inlet dimensions, and other factors create a net movement of water into one inlet and a net movement of water out of a nearby inlet. Offshore of the VCR, annual representative significant wave height is ~1.3 m, wave period is ~7 s, and wave direction is ~82° with respect to the north (Wiberg *et al*, 2015). Waves and tides set up an alongshore current and sediment transport that interacts with the suspended sediment exchange between bays and ocean, which is modelled in the following section.

Model description

Delft3D-SWAN couples the computation of hydrodynamics with sediment transport and vegetation. Here, a water and sediment mass balance is carried out in two dimensions throughout the entire modelled system, and alternate realizations are run to determine the sediment exchange between the bay and the ocean, under the influence of wind waves and tide, taking into account the presence of vegetation that affects residence times and sediment deposition. The flow resistance effects of vegetation are implemented through depth-integrated computations, formulated in accordance with the equations proposed by Baptist (2005). Defining a coordinate system with the *x*-axis longitudinal, the *y*-axis transversal, and the *z*-axis vertical upward, the system of shallow water equations governing fluid flow is:

$$\frac{\partial U}{\partial t}+U\frac{\partial U}{\partial x}+V\frac{\partial U}{\partial y}= -g\frac{\partial \eta}{\partial x}+g\frac{U\left(U^2+V^2\right)^{1/2}}{C_b h}+\frac{\partial}{\partial x}\left(v_H\frac{\partial U}{\partial x}\right)+\frac{\partial}{\partial y}\left(v_H\frac{\partial U}{\partial y}\right) \quad (1)$$

$$\frac{\partial V}{\partial t}+U\frac{\partial V}{\partial x}+V\frac{\partial V}{\partial y}= -g\frac{\partial \eta}{\partial y}+g\frac{V\left(U^2+V^2\right)^{1/2}}{C_b h}+\frac{\partial}{\partial x}\left(v_H\frac{\partial V}{\partial x}\right)+\frac{\partial}{\partial y}\left(v_H\frac{\partial V}{\partial y}\right) \quad (2)$$

$$\frac{\partial \eta}{\partial t}+\frac{\partial U}{\partial x}+\frac{\partial V}{\partial y}=0 \quad (3)$$

where U and V are the velocities in the x and y directions, η is the elevation of the water surface, h is the water depth, C_b is the Chezy bed roughness, g is the gravity acceleration, and v_H is the horizontal eddy viscosity.

The sediment-transport and morphology modules in Delft3D simulate bedload and suspended-load fluxes of cohesive and non-cohesive sediments and the exchange of sediment between the bed and water column. The transport of each sediment class is calculated separately, taking into account the availability of each fraction in the bed. Bedload transport for non-cohesive sediment is computed with the formula of van Rijn (1993). Erosion and deposition shear stresses for sediment resuspension are based on the Shields parameter, while suspended load transport is calculated by solving the advection–diffusion equation:

$$\frac{\partial c}{\partial t}+U\frac{\partial c}{\partial x}+V\frac{\partial c}{\partial y}=\frac{\partial}{\partial x}\left(\varepsilon_s\frac{\partial c}{\partial x}\right)+\frac{\partial}{\partial y}\left(\varepsilon_s\frac{\partial c}{\partial y}\right)+\frac{c_{eq}-c}{T_s} \quad (4)$$

where c is the suspended sediment mass concentration, ε_s is the sediment eddy diffusivity, T_S is an adaptation time scale, and c_{eq} is the local equilibrium depth-averaged SSC. For cohesive sediments, the Partheniades–Krone formulations for erosion and deposition are used (Partheniades, (1965). In these formulations, the critical shear stress for erosion is always greater than or equal to the one for deposition; therefore, intermediate shear–stress conditions may exist for which neither erosion nor deposition occurs (see Delft3D manual for full reference, https://oss.deltares.nl/web/delft3d/manuals).

In the SWAN model, wind waves are described with the wave action density spectrum in the two-dimensional geographic space (Booij *et al*, 1999) and SWAN is designed to simulate random, short-crested waves in coastal regions with

shallow water. The model accounts for wave generation, dissipation through whitecapping (Komen *et al*, 1984), bottom friction (Hasselmann and Olbers, 1973), and depth-induced breaking (Battjes and Janssen, 1978), and nonlinear wave–wave interactions. For computational reasons, the model is set up on the same square grid as the Delft3D model, with a 250m cell size.

The processes by which waves affect currents and vice versa are taken into account in our simulations, with an online coupling between the SWAN and Delft3D modules. In the case of waves coming from the direction opposite to a current, the radiational stresses produced by the dissipation of wave energy by bottom friction tend to decrease the momentum of the current. The presence of waves also enhances the mean shear stress on the bed. This enhancement is caused by the nonlinear interaction between the boundary layers at the bed associated with the waves and the current (Grant and Madsen, 1979). The enhancement of the mean shear stress is modelled using Soulsby *et al*'s (1993) formula:

$$\tau_m = \tau_c \left[1 + 1.2 \left(\frac{\tau_w}{\tau_w + \tau_c} \right)^{3/2} \right] \tag{5}$$

where τ_m is the combined waves/current bed shear stress, τ_c is the bed shear stress due to the current alone:

$$\tau_c = \frac{g \rho u |u|}{C^2} \tag{6}$$

and τ_w is the bed shear stress due to waves:

$$\tau_w = \frac{1}{2} \rho f_w {u_b}^2, \quad u_b = \frac{\pi H_s}{T_p \sinh(KD)}, \; K = \frac{2\pi}{c T_p} \tag{7}$$

where u_b is the significant wave bottom orbital velocity, K is the wave number, D is the channel and domain depth, T_p is the wave peak period, and f_w is a friction coefficient, computed as:

$$f_w = \begin{cases} 0.251 \exp\left[0.521 \left(\frac{u_b}{\omega K_s} \right)^{-0.19} \right] & , \frac{u_b}{\omega K_s} > \frac{\pi}{2} 0.3, \frac{u_b}{\omega K_s} < \frac{\pi}{2} \end{cases}. \tag{8}$$

where K_s is the Nikuradse roughness, estimated as 3.5 times the median grain size. In addition, because of the extra turbulence generated close to the bed, the whole current profile is modified by the presence of waves. This second effect is equivalent to an enhancement of the apparent bed roughness (Grant and Madsen, 1979).

Finally, the presence of currents affects waves by modifying their celerity:

$$c_a = c_r + u \tag{9}$$

where c_a is the absolute celerity and c_r is the relative celerity. Currents flowing in the opposite direction of wave propagation tend to decrease wave period and group velocity and, if the wave action is conserved, to increase wave height.

Effect of vegetation on flow

The Delft3D model allows users to specify bed roughness and flow resistance on a sub-grid level by defining various land use or roughness classes. One way to model vegetation in Delft3D is to correct the bed roughness using the equation proposed by Baptist (2005). Baptist's formulation is based on the concept that vegetation can be modelled as rigid cylinders characterized by height h_v, vegetation density n, stem diameter D, number of stems per square metre m, and drag coefficient C_D. Various combinations of vegetation parameters can represent diverse wetland configurations under different water flow conditions. In this formulation, the velocity profile is divided into two flow zones: (1) a zone of constant flow velocity, u_v, inside the vegetated part and (2) a logarithmic velocity profile, u_u, above the vegetation starting from the velocity value u_v at the vegetation interface.

Setup of hydrodynamic model

We simulate water flow and sediment transport on a computational grid of 150×459 cells, each 250×250m in size (Figure 2). To set up, test, and validate our modelling framework we used extensive datasets collected in the VCR and available through the VCR-LTER website. The data encompass long-term measurements of water level (Hog Island station: VCR97053), sediment transport (Wiberg *et al*, 2015), salt marsh accretion, and vegetation characteristics within the salt marshes (Apollone, 2000), which are presented in detail in the following.

The VCR topography and bathymetry were extracted from existing digital elevation models (DEMs) (e.g. Oertel *et al*, 2000; Richardson *et al*, 2014) and grids used in previous modelling studies (e.g. Mariotti *et al*, 2010; Safak *et al*, 2015; Wiberg *et al*, 2015). Where these detailed data sources did not provide coverage or good data quality, the bathymetry was based on local surveys and on NOAA charts. Depths outside the VCR were gathered from NOAA charts and datasets. The compiled dataset was interpolated, where necessary, to ensure that the main channels connecting the bays within the system were represented. Initial test runs showed that the domain size allows wave propagation. The simulated tide along the three open boundaries north, east, and south (Figure 2) is obtained by superimposing the various tidal harmonics with their corresponding phases and amplitudes (Figure 3a), recorded from the NOAA station in Hog Island (VA). A no-flow condition is imposed at the landward boundaries.

Waves in the model are generated at the ocean boundaries and by local winds. We use data and wind statistics from the NOAA weather station at Wachapreague in Virginia, USA, based on observations between July 2008 and September 2017. These observations show that the most frequent wind direction in the VCR is from the SSW (Figure 2). We use a steady wave field with a mean annual wind speed of $6\,m\,s^{-1}$ from the SSW direction, neglecting coupling with currents.

We use the sediment bottom distribution measured in the VCR by Wiberg *et al* (2015), which includes fine sand (D_{50}= 125μm; sediment density ρ = $2650\,kg\,m^{-3}$; dry bed density ρ_d=$800\,kg\,m^{-3}$), silt (D_{50}=20μm, settling velocity w_s= $0.1\,mm\,s^{-1}$), and mixed silt–very fine sand (D_{50}= 63μm, settling velocity w_s= $3.0\,mm\,s^{-1}$) (see also Castagno *et al*, 2018; Nardin *et al*, 2018). Starting from an initial uniform sediment distribution in the bay domain, we run the model until it reaches a steady state for the non-cohesive sediments and the two classes of cohesive sediment. We define this state as the point at which the SSC is stable in time.

The suspended sediment eddy diffusivities are calculated using horizontal large-eddy simulations and grain settling velocity (see Delft3D manual for full reference). The horizontal eddy-viscosity coefficient is computed from a horizontal large-eddy simulation, and the background horizontal viscosity here is set equal to $1\,m^2\,s^{-1}$. Bed roughness is set to a spatially

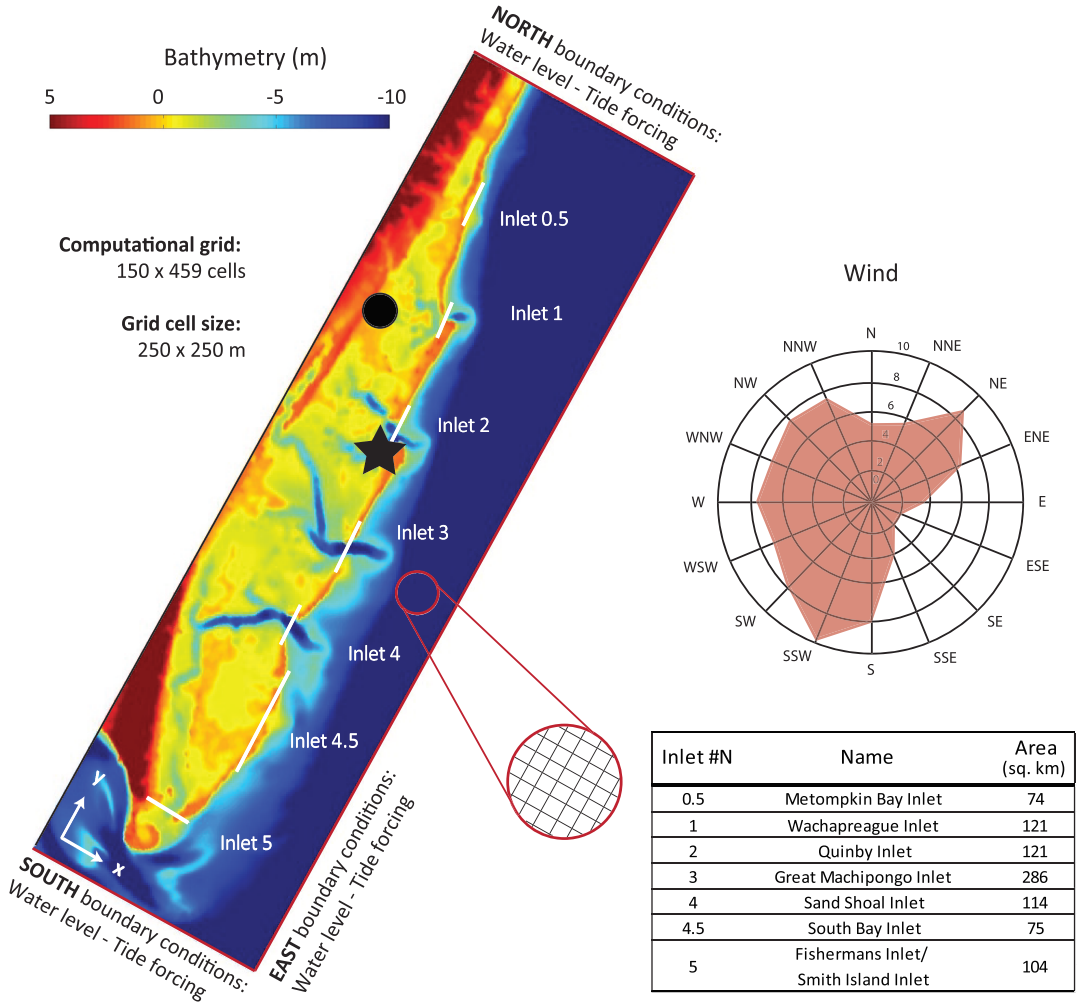

Inlet #N	Name	Area (sq. km)
0.5	Metompkin Bay Inlet	74
1	Wachapreague Inlet	121
2	Quinby Inlet	121
3	Great Machipongo Inlet	286
4	Sand Shoal Inlet	114
4.5	South Bay Inlet	75
5	Fishermans Inlet/ Smith Island Inlet	104

Figure 2. Numerical domain with boundary conditions; the colour map shows elevation extracted from existing DEMs (e.g. Oertel *et al*, 2000; Mariotti *et al*, 2010) and grid used in previous studies; white lines highlight the cross-sections of the inlet channels used for quantifying water and sediment fluxes. The black star indicates the location of NOAA station VCR97053 (Hog Island, VA). The wind rose shows the yearly wind direction measured by the NOAA station at Wachapreague (VA), USA in the black circle. The table shows VCR bay names and characteristics. [Colour figure can be viewed at wileyonlinelibrary.com]

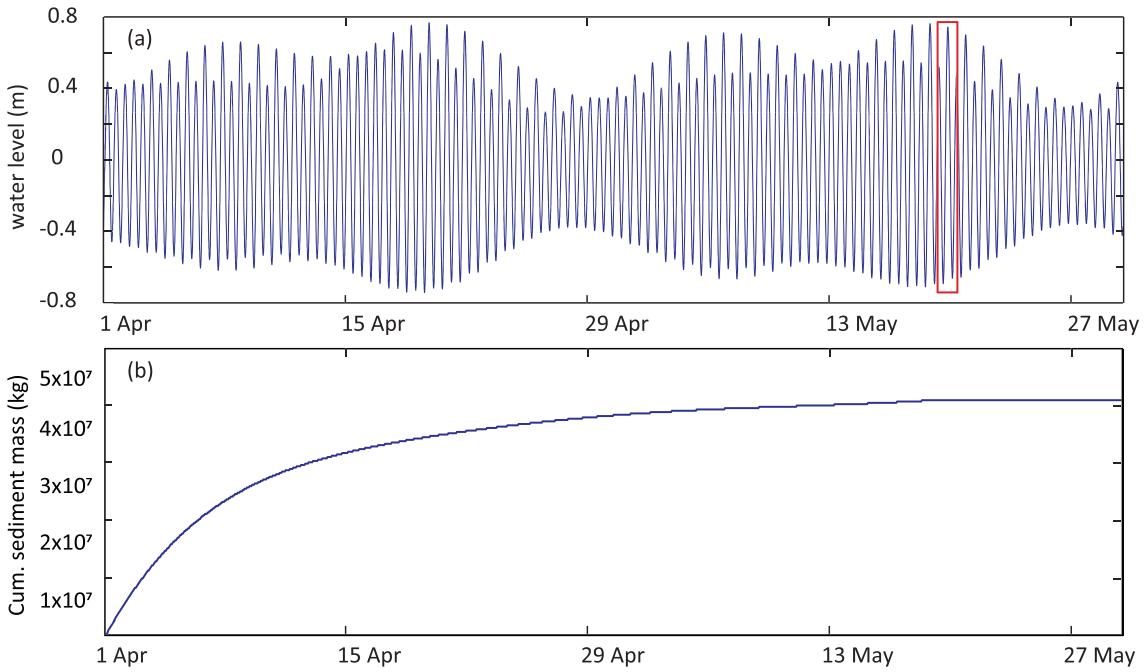

Figure 3. (a) Water level simulated in the VCR estuary. The red box shows the focus interval used to present the study's results. (b) Cumulative sediment mass over the simulation time, calculated at Great Machipongo Inlet, stabilizes in correspondence with the time interval used to present our results and analysis. [Colour figure can be viewed at wileyonlinelibrary.com]

and temporally constant Chézy value of 65 $m^{1/2}$ s^{-1}. A time step of 60 s is adopted to satisfy all stability criteria.

Vegetation plays an important role in sediment deposition (D'Alpaos *et al*, 2007). In the 1930s, the seagrass in the VCR completely disappeared and the bays changed from a highly productive seagrass-dominated system to an algae-dominated system (McGlathery *et al*, 2001). Recent restoration activities have reintroduced seagrass (McGlathery *et al*, 2012; Reynolds *et al*, 2012), with seagrass meadows currently occupying 25 km^2 of the bays.

To understand how the vegetation influences sediment trapping and sediment budget exchange, we simulate the test cases indicated in Table 1. We consider two species of vegetation (*S. alterniflora*, *Z. marina*) in the VCR, based on orthophotogrammetry and field data (aerial photographs courtesy of Google Earth; Apollone, 2000; Wiberg *et al*, 2015; Sun *et al*, 2018). Within each vegetation community, vegetation characteristics are assumed to be uniform, with a given height, density, and stem diameter consistent with measurements acquired within *S. alterniflora* and *Z. marina* communities (McGlathery *et al*, 2001) and classification map based on Landsat images (Sun *et al*, 2018). In particular, *S. alterniflora* in this region is characterized by stem height h_v=0.7 m and vegetation density n=2 m^{-1}, and for *Z. marina* h_v=0.3 m and n=4 m^{-1} (the vegetation density $n = mD$, where D is the stem diameter and m is the number of stems per square metre; see Nardin *et al*, 2018). For example, we investigate the effects of seasonality by comparing h_v = 0.7 m and n = 2 m^{-1}, representing winter, and h_v=1.4 m and n = 4 m^{-1}, representing summer for *S. alterniflora* (Nardin *et al*, 2018). To explore the seasonality effects by *Z. marina,* we compared values of h_v= 0.3 m and n=4 m^{-1} during winter with h_v=0.6 m and n= 8 m^{-1} to represent summer time (Nardin *et al*, 2018).

Offshore wave conditions

We retrieved offshore wave statistics from the NOAA Wave Watch 30-year reanalysis hindcast (Chawla *et al*, 2013). Based on the occurrence of different wave heights and wave directions, we selected 25 representative model conditions (Figure 4, Table 1). We vary the significant wave heights (0.6, 0.8, 1, 1.3, 1.6 m), approach directions (40, 60, 82, 110, 130° from the north), and keep the wave period constant at 7 s. Considering the wave-driven alongshore transport of sediments, annual representative conditions are a significant wave height of ~1.3 m, a wave period of ~7 s, and a wave direction of ~82° with respect to the north (Run ID: VCR1382). For convenience, in our results section, we refer to the 'relative' impact angle φ_R, calculated with respect to the coastline (Figure 6a, Table 1).

In our study, deep water waves are prescribed at the offshore boundaries with a 10° directional spread and a JONSWAP frequency spectrum. The computed wave field from SWAN is updated after every 60 min of simulated Delft3D flows.

Model validation

We use measured tide data recorded from the NOAA station of Hog Island, VA to validate and calibrate our numerical model. We processed data from Hog Island station because of its proximity to the open ocean, its central location in the barrier system, and because this is the largest bay with extensive seagrass beds and salt marshes.

We calibrated the model by adjusting the water-level forcing, phase, and amplitude at the southern, northern, and eastern open boundaries to match measured water levels at NOAA station VCR97053 (Hog Island, VA) from 10 to 17 February 2004.

Table 1. Variables and boundary conditions used in Delft3D to run our numerical experiments (see text for vegetation parameters selection). The h_v value shows a vegetation height for salt marsh used in the specific run, while the second value represents a vegetation stem length for SAV. In the same way, n characterizes the value of vegetation density for salt marsh and the second value is proposed for SAV. φ_R is the 'relative' impact angle, calculated with respect to the coastline

Model runs without vegetation					Model runs with vegetation				
Run ID:	H_S (m)	φ_R (°)	h_v (m)	n (m^{-1})	Run ID:	H_S (m)	φ_R (°)	h_v (m) (salt marsh-SAV)	n (m^{-1}) (salt marsh-SAV)
VCR0000	–	–	–	–	VCR0640V	0.6	11	0.7–0.3	2–4
VCR0640	0.6	11	–	–	VCR0840V	0.8	11	0.7–0.3	2–4
VCR0840	0.8	11	–	–	VCR1040V	1	11	0.7–0.3	2–4
VCR1040	1	11	–	–	VCR1340V	1.3	11	0.7–0.3	2–4
VCR1340	1.3	11	–	–	VCR1640V	1.6	11	0.7–0.3	2–4
VCR1640	1.6	11	–	–	VCR0660V	0.6	31	0.7–0.3	2–4
VCR0660	0.6	31	–	–	VCR0860V	0.8	31	0.7–0.3	2–4
VCR0860	0.8	31	–	–	VCR1060V	1	31	0.7–0.3	2–4
VCR1060	1	31	–	–	VCR1360V	1.3	31	0.7–0.3	2–4
VCR1360	1.3	31	–	–	VCR1660V	1.6	31	0.7–0.3	2–4
VCR1660	1.6	31	–	–	VCR1360V	0.6	53	0.7–0.3	2–4
VCR1360	0.6	53	–	–	VCR1660V	0.8	53	0.7–0.3	2–4
VCR1660	0.8	53	–	–	VCR0682V	1	53	0.7–0.3	2–4
VCR0682	1	53	–	–	VCR1382V	1.3	53	0.7–0.3	2–4
VCR1382	1.3	53	–	–	VCR1082V	1.6	53	0.7–0.3	2–4
VCR1082	1.6	53	–	–	VCR06110V	0.6	81	0.7–0.3	2–4
VCR06110	0.6	81	–	–	VCR08110V	0.8	81	0.7–0.3	2–4
VCR08110	0.8	81	–	–	VCR10110V	1	81	0.7–0.3	2–4
VCR10110	1	81	–	–	VCR13110V	1.3	81	0.7–0.3	2–4
VCR13110	1.3	81	–	–	VCR16110V	1.6	81	0.7–0.3	2–4
VCR16110	1.6	81	–	–	VCR06130V	0.6	101	0.7–0.3	2–4
VCR06130	0.6	101	–	–	VCR08131V	0.8	101	0.7–0.3	2–4
VCR08131	0.8	101	–	–	VCR10132V	1	101	0.7–0.3	2–4
VCR10132	1	101	–	–	VCR13133V	1.3	101	0.7–0.3	2–4
VCR13133	1.3	101	–	–	VCR16134V	1.6	101	0.7–0.3	2–4
VCR16134	1.6	101	–	–	VCR0000VV	–	–	1.4–0.6	4–8

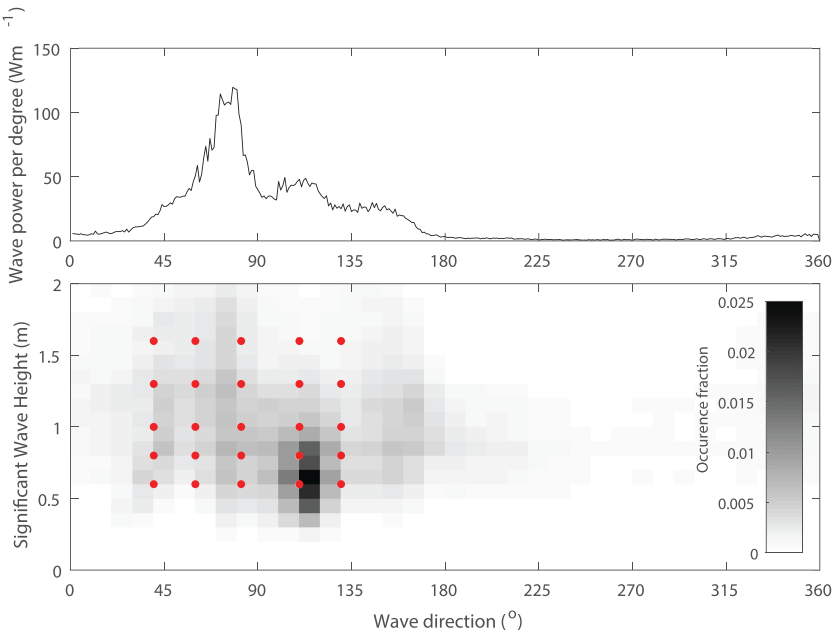

Figure 4. Co-occurrence of wave directions and heights offshore of the VCR, including the directional distribution of wave power. Red markers represent the conditions simulated in our study (Table 1). The greyscale colour shows the frequency of wave condition co-occurrence. [Colour figure can be viewed at wileyonlinelibrary.com]

An agreement among field measurements and numerical model, both in tidal amplitude and tidal phase, was obtained when imposing a water-level signal delayed 72 min and dampened by a factor of 88%.

To validate our model runs, we used water levels at Hog Island station during the winter time, from 24 February to 1 March 2004 (Figure 5). The coherence between the model and measurements was analysed by the model efficiency (ME =0.99), root mean square error (RMSE=0.084 m), correlation coefficient (R =0.99), and model performance (skill, S=0.99). To better understand seasonality effects on the model result, we conducted a summer-time model validation, from 20 to 26 August 2004 (Figure 5b). Those results have shown agreement among numerical model results and water-level measurements with correlation coefficient (R=0.99) and model performance (S=0.99).

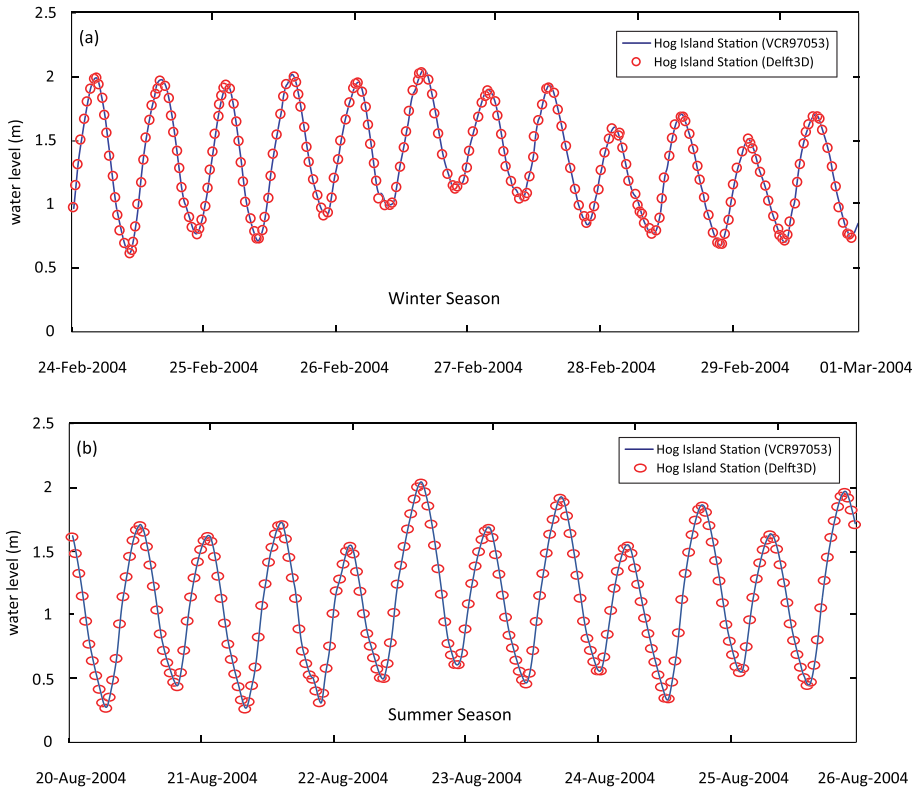

Figure 5. Comparison between modelled and measured water levels. (a) Winter season: computed (red circle) and measured (blue line) water levels at NOAA station VCR97053 (Hog Island, VA). (b) Summer season: computed (red ellipse) and measured (blue line). The model is validated along the time with measurements of water level. [Colour figure can be viewed at wileyonlinelibrary.com]

Results

Effect of waves on bay hydrodynamics

To quantify the amount of water flowing into the bay through the tidal inlets, we studied the water-level profile as a function of the velocity during two idealized tidal cycles from 20 to 21 May (Figure 3a). We chose this period to limit the effects of model spin-up on our results, and to focus on tidal cycles in which the bays reach a steady state (Figure 3b).

Plotting the water level against velocity (tidal stage plot) allows comparison of the magnitude of the flood currents relative to the ebb currents at every considered stage of tide. Figure 6b shows that, for each tidal cycle, the maximum flow velocity is greater during ebb (~0.8 m s^{-1}) than during flood (~0.6 m s^{-1}). Assessing the impact of waves on bay hydrodynamics, we find that the ebb dominance of tidal inlets is not strongly dependent on offshore wave direction (φ_R) (Figure 6b). The maximum ebb and flood velocities are not constant for the two different tidal cycles, because of the mixed semidiurnal tidal range (Figure 3). The difference in ebb velocities in Figure 6c is −0.82 m s^{-1} on the first ebb tide, then −0.80 m s^{-1} on the second ebb tide, which highlights a not substantial difference between the two selected tidal cycles. Similarly, flood velocities show analogous behaviour, with 0.59 m s^{-1} on the first flood tide and 0.62 m s^{-1} on the following one (Figure 6c).

To further analyse the influence of waves on the tidal inlets' hydrodynamic and flood/ebb dominance, we define:

$$U_F = \frac{u_{max,\ waves}}{u_{max,\ no\ waves}} \tag{10}$$

$$U_E = \frac{u_{min,\ waves}}{u_{min,\ no\ waves}} \tag{11}$$

where $u_{max,waves}$ and $u_{min,waves}$ represent, respectively, the maximum (flood) and minimum (ebb) velocity simulated at the inlets in the presence of waves, normalized with $u_{max,\ no\ waves}$ and $u_{min,no\ waves}$, the corresponding values in the absence of waves.

In both cases, U_F and U_E decrease for high waves and increase when the angle is more shore-normal (Figure 7), but variations are less than 1%. Referring to the angles notation indicated in Figure 6, the wave characterized by H_S = 1.3 m and φ_R = 81° slightly reverses the trend, because the wave direction is opposite to the jet from the inlet and this might generate jet instability processes (Figures 7a, c, and d).

Effect of waves on the alongshore current

The alongshore current calculated at the transversal cross-section, in the midway between Great Machipongo Inlet and Sand Shoal Inlet, is plotted in Figure 8 as a function of the significant wave height for different directions. The linear correlation shown by the regression lines underlines that with increasing wave height, the alongshore current proportionally increases. Generally, the alongshore current velocity is at the maximum value when the relative wave direction is around 45° (Ashton and Giosan, 2011). This wave direction is approximately represented by the angle of 53° in the VCR coastline morphology.

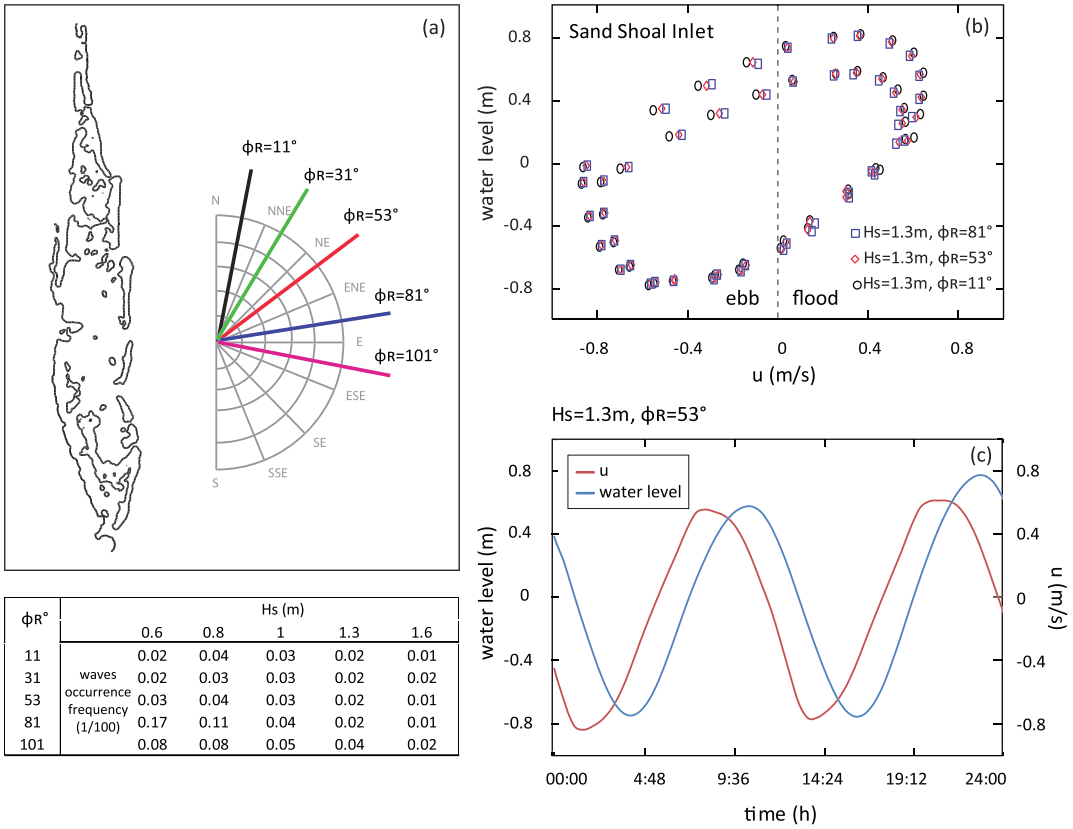

ϕR°		Hs (m) 0.6	0.8	1	1.3	1.6
11	waves occurrence frequency (1/100)	0.02	0.04	0.03	0.02	0.01
31		0.02	0.03	0.03	0.02	0.02
53		0.03	0.04	0.03	0.02	0.01
81		0.17	0.11	0.04	0.02	0.01
101		0.08	0.08	0.05	0.04	0.02

Figure 6. (a) Sketch of the VCR coastline and the relative wave directions considered in our model; (b) tidal stage plots calculated at Sand Shoal Inlet for two tidal cycles of the data extracted from the model, considering the significant wave height of 1.3 m and three different wave directions approaching the shore; (c) instantaneous water level and *x*-component of velocity flowing into the bay through a tidal inlet at the same time. [Colour figure can be viewed at wileyonlinelibrary.com]

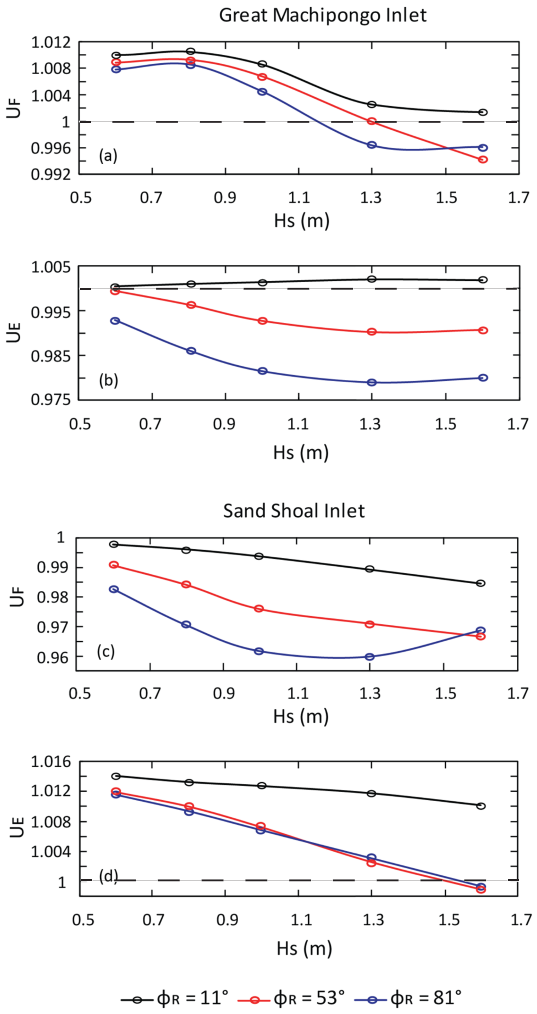

Figure 7. Normalized *x*-component velocity U_F and U_E as a function of the wave height at Great Machipongo Inlet (a, b) and Sand Shoal Inlet (c, d) for different values of wave directions. The black dashed lines represent the value of the U_F and U_E ratios equal to 1. [Colour figure can be viewed at wileyonlinelibrary.com]

Figure 9 shows the alongshore current computed along the transversal cross-section between Great Machipongo Inlet and Sand Shoal Inlet. Data are plotted for the same two tidal cycles considered in our results section (Figure 3). The alongshore current without waves (black line) is compared to the case of different-height waves with the same origin direction (Figure 9a) and to the case of different direction angles with the same wave height (Figure 9b). Our results show that the presence of offshore waves from the north direction increases currents towards the south (Table 2). For the same angle of 53°, as the significant wave height increases, the alongshore current slightly enhances towards the south (Figure 9a). Figure 9b shows that a minimum value of alongshore current occurs when the waves impact the shoreline at an angle of 53°. This result highlights the most impactful condition for the development of the alongshore current towards the south.

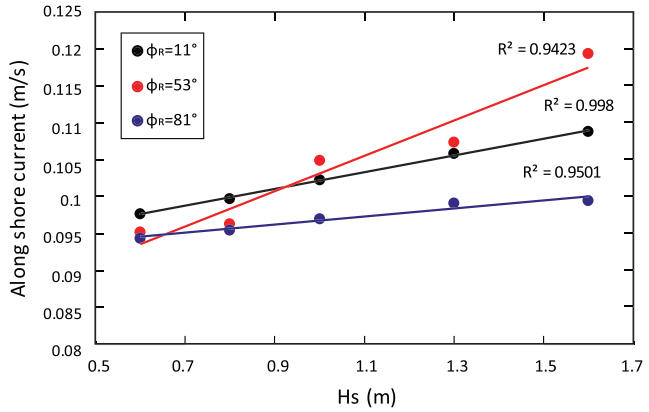

Figure 8. Alongshore current as a function of H_S in the transversal section between Great Machipongo Inlet and Sand Shoal Inlet and regression lines for different wave directions. [Colour figure can be viewed at wileyonlinelibrary.com]

Effect of waves on sediment transport during ebb and flood

The sediment budget inside the VCR is primarily determined by SSC at flood and ebb flow through the tidal inlets. To understand the coupling between SSC and the alongshore current, we plotted in Figure 10 the SSC for mud (20 μm) with the corresponding depth-averaged velocity field.

We found that the ebb velocity simulated at Great Machipongo and Sand Shoal Inlets decreases in the presence of waves (Figure 10), because waves interfere with the outgoing currents. In contrast, the flood velocity increases when waves approach the coastline (Figure 10c), because the waves promote the incoming currents. The suspended sediment emitted from the inlets results in higher concentration under-wave action, and the alongshore current transports the sediment adjacent to the coastline.

Alongshore current impacts on sediment budget

Wave direction and energy directly impact the development of alongshore currents, as shown in Figure 8. Subsequently, the effects of alongshore currents on sediment circulation inside and outside the bay are highlighted and summarized.

To analyse the SSC through the bays, we define:

$$S_F = \frac{SSC_{waves}}{SSC_{no\ waves}} \tag{12}$$

where SSC_{waves} is the cumulative SSC calculated after 2 months of numerical simulation in the presence of waves normalized by $SSC_{no\ waves}$, the respective cumulative SSC in the case without waves.

In Figure 11, we plot S_F varying with the relative angle of wave approach, referring to the representative wave of significant height at 1.3 m. The sediment flux S_F is represented as a function of the relative wave angle, varying the wave height as related to two tidal inlets, Great Machipongo (Figure 11a) and Sand Shoal Inlets (Figure 11b). Our experiments focus on these two inlets because they show the larger amount of sediment exchange between VCR coastal bays and the ocean (Table 3). The sediment flux decreases for high values of significant wave height, and the curve minimum occurs when the relative wave direction is around 53°, which is when the alongshore current velocity reaches the maximum value. Model conditions with alongshore current at the maximum values represent the worst conditions for the re-entry of sediment into the bay. In fact, if the sediment flows out through the inlet and the alongshore current is at the maximum value, the sediment is partially transported to the adjacent tidal inlet in the direction of the alongshore current, however, sediment could in part be transported back into the lagoon.

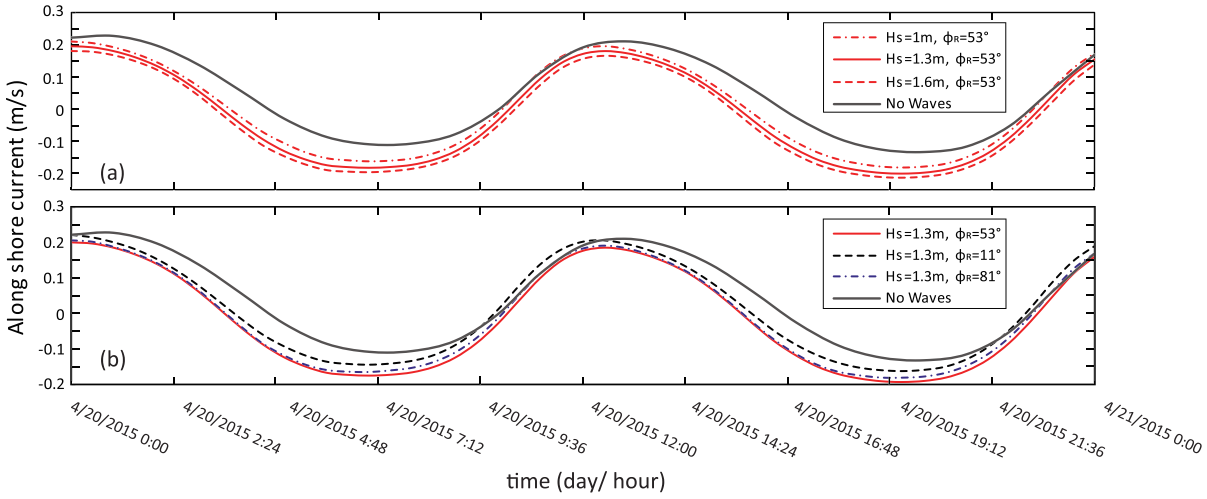

Figure 9. Alongshore current as a function of tidal level (two tidal cycles) calculated at the transversal cross-section between Great Machipongo Inlet and Sand Shoal Inlet at 100m from the shoreline, varying the wave height (a) and the origin direction (b). [Colour figure can be viewed at wileyonlinelibrary.com]

The impact of vegetation on sediment retention is a key process to maintain sediment availability in the bay. We calculated, for tidal inlets and cross-sections located between every inlet, the mass of suspended sediment exported from VCR bays (Table 3). During the winter, the normalized suspended sediment mass exiting the bays is higher than in the summer, when vegetation (seagrasses and salt marshes) density and height are typically greater (Figure 12).

Discussion

Comparison with previous works

Our study reveals the pivotal role of seasonal vegetation growth combined with waves and tidal currents on the VCR multiple tidal inlet systems. Indeed, those processes alter the hydrodynamics and sediment fluxes in coastal bays through each tidal inlet. Our study reveals that the ebb dominance of the bay system is not strongly affected by the presence of offshore waves (Figures 6 and 7). In particular, the ratios U_F and U_E quantify the effects of offshore waves on tidal fluxes, respectively, during flood and ebb compared to the study case without waves. Changing the wave angle (ϕ_R) and significant wave height (H_S), our model runs show a variation in velocity at the tidal inlet with values between 1 and 4% compared to the case without waves (Figure 7). Therefore, our study shows the low

Table 2. Alongshore current values from Figure 9. Velocities from the no-waves condition are at the bottom of the table, while the values show combinations of wave direction and significant wave height. Each model run shows a maximum and minimum value due to the tidal flux influence

Significant wave height [H_S (m)]	Wave direction [ϕ_R (°)]	Alongshore current max (ms^{-1})	Alongshore current min (ms^{-1})
1	53	0.21	−0.18
1.3	53	0.20	−0.20
1.6	53	0.18	−0.21
1.3	11	0.22	−0.16
1.3	81	0.20	−0.19
No-waves condition		0.23	−0.14

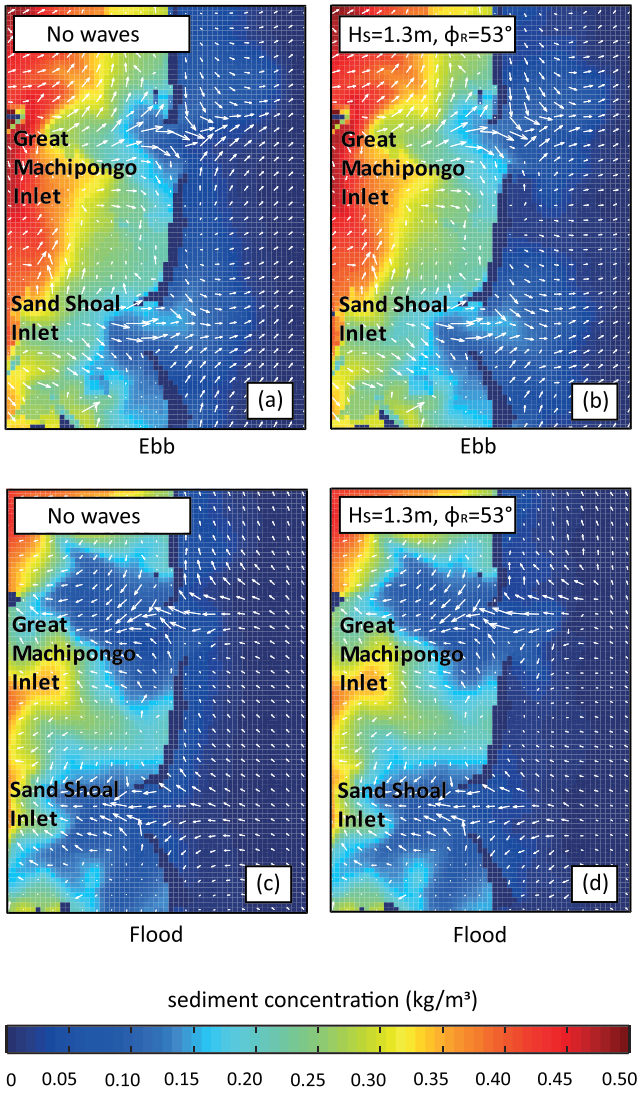

Figure 10. Contour map of the SSC (20μm) simulated for Great Machipongo Inlet and Sand Shoal Inlet at two different times: during ebb in absence of waves (a) and with the test case wave characteristics (b), during flood without waves (c) and in the presence of the test case waves (d). White arrows indicate directions and intensities of the corresponding depth average velocity. [Colour figure can be viewed at wileyonlinelibrary.com]

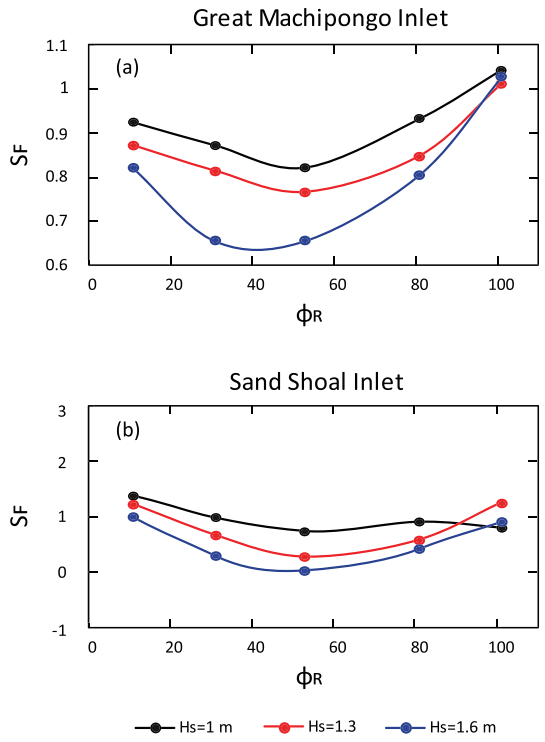

Figure 11. Sediment flux plotted as a function of the relative wave directions at Great Machipongo Inlet (a) and Sand Shoal Inlet (b) for different wave heights. [Colour figure can be viewed at wileyonlinelibrary.com]

impact of offshore waves on tidal inlet velocities. However, the energetic waves with H_S = 1.6m decrease the ebb and flood velocities in the inlet, with higher values for the wave with angles between ϕ_R= 53° and 81° (Figure 7). Similarly, Figures 8 and 9 display the impact of the offshore waves on the alongshore current, with higher values for the case ϕ_R= 53° and H_S>0.8m. Also, increasing the wave's energy enhances the velocity alongshore (Figure 8). Moreover, U_F and U_E at both tidal inlets always show low values (Figure 7) with larger H_S, because they are impacted by the increased alongshore currents generated by the offshore waves (Figure 8). Those effects at Great Machipongo Inlet are able to switch U_F from positive to negative values (Figure 7a).

Sediment export from the bays is one of the most important parameters that can help to define VCR bays' sediment budget and long-term evolution. Figure 10 shows the effects of offshore waves during the phases of ebb and flood on the sediment concentration around the tidal inlets. We quantify with S_F the export of sediment with offshore waves compared to the model runs without waves. Wave direction has an important role in sediment exiting the bays, in fact, tidal inlets show a lower export of sediment for ϕ_R= 53° (Figure 11). In contrast, the alongshore current shows a maximum value for ϕ_R= 53° (Figure 8), which implies that most of the sediment exported from the inlets is transported along the shoreline. This hydrodynamic and sediment transport result suggests that stronger waves reduce the export of sediment from the bays. The amount of sediment exiting the inlets moves along the shoreline, and it might reach and re-enter the subsequent inlet.

Inside coastal bays the sediment transport is influenced by the presence of vegetation, wind waves, and tidal hydrodynamics. Previous studies have noted that sediment resuspension in the VCR bays (tidal flats, channels, etc.) is governed by wind waves (Lawson *et al*, 2007; Mariotti *et al*, 2010). In fact, locally generated wind waves are controlled by fetch and water depth, which, in turn, control sediment resuspension. This resuspension mechanism, combined with tidal fluxes, determines the sediment exchange with the ocean and whether subaqueous tidal flats erode or aggrade in time (Chauhan, 2009). In the VCR, sediment contributions from offshore sources and river discharge are small (Boon and Byrne, 1981; Nichols and Boon, 1994). The main sediment source for the VCR is represented by the sediment expelled from other neighbouring Delmarva Estuaries and Chesapeake Bay, but during the 20th century, the volume of this sediment decreased (Cooper, 1995). Sediment availability for deposition is fundamental because the VCR does not have any tributaries that deliver sediment to the bay, but most of the sediment transport, erosion, and depositional processes are related to sediment redistribution within the system.

Mariotti and Fagherazzi (2013) showed that marsh collapse could occur if there is positive feedback between marsh and tidal flat erosion and wave generation in tidal flats. Lack of sediment supply creates deeper tidal flats and hinders marsh progradation.

Our model suggests that vegetation seasonally affects the suspended sediment exchange between VCR bays and the ocean (Figure 12). In particular, during the summer, when there is a greater vegetation biomass, more sediment is trapped in the bays – up to 10% more compared to the case without vegetation (Nardin *et al*, 2018).

The sediment budget of a given system is often considered an indicator of coastal stability. Our results show that the suspended sediment tends to be exported from the tidal basins. Ganju *et al* (2013) suggested that marsh systems with a net export of sediment can be more unstable than systems with net import of sediment. Castagno *et al* (2018) showed that as storm events increase in intensity, more sediment is transported into tidal bays, thereby increasing the resilience. In contrast,

Table 3. Sediment exported from each VCR bay divided by monitored inlet. Exported tons from each bay without and with offshore wave condition, with H_S=1.3 m and φ_R=53°. Sediment exchange is quantified with the ratio (R_w and R_s) between the suspended sediment mass (20 μm) calculated in the presence of waves and the corresponding suspended sediment mass without waves, expressed in tons. R_w represents vegetative conditions during winter, while R_s shows vegetation during summer

Name of bay	Model inlet ID	Exported tons (no waves)	Exported tons (winter, with waves)	R_w	Exported tons (summer, with waves)	R_s
Metompkin Bay	0.5	−7.71	−9.12	1.18	−8.08	1.05
Wachapreague	1	−2.01	−3.42	1.70	−2.18	1.08
Quinby	2	−30.59	−22.84	0.75	−21.12	0.69
Great Machipongo	3	−4.29	−33.96	7.92	−5.51	1.29
Sand Shoal	4	−13.79	−50.75	3.68	−15.22	1.10
South Bay	4.5	−11.26	−23.59	2.10	−10.95	0.97
Fishermans	5	−56.17	−142.96	2.55	−55.50	0.99

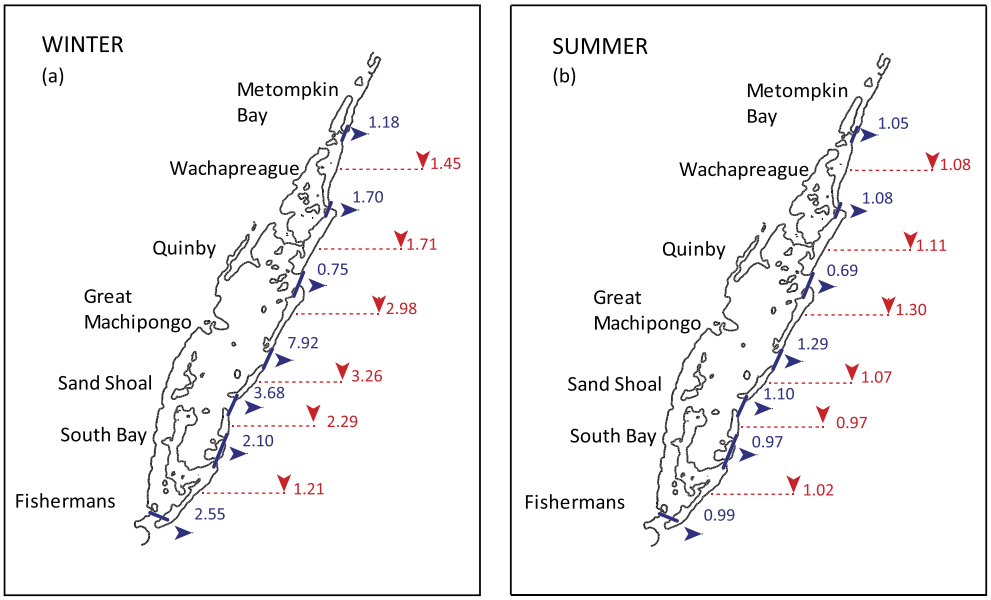

Figure 12. Conceptual model of the effect of waves on the sediment exchange between bays during winter (a) and summer (b) considering the presence of waves with H_S=1.3 m and φ_R=53°, varying vegetation characteristics inside the bays. Sediment exchange is quantified with the ratio between the suspended sediment mass (20 μm) calculated in the presence of waves and the corresponding suspended sediment mass without waves, expressed in tons. Blue and red numbers in the figure represent respectively the amount of sediment coming through tidal inlets and transversal cross-sections between each bay, and arrows suggest the sediment direction. [Colour figure can be viewed at wileyonlinelibrary.com]

storms can rip up and erode marshes, especially on the marsh platform boundary where plants are more exposed to the wave's energy (Marani *et al*, 2011). In particular, storms provide the material necessary to counteract rising sea levels (Mariotti *et al*, 2010). Interactions between vegetation species and SSC will likely play an important role in determining how coastal wetlands respond to sea level rise and changes in storm frequency and energy in the future.

Model limitations

Delft3D-SWAN operates in two dimensions, depth-averaged for the hydrodynamic computational field. It is therefore unable to address vertical components such as vertical sediment and water re-mixing, salinity gradient, and stratifications. Hydraulic roughness due to vegetation is modelled in a variety of ways in Delft3D. For rigid vegetation, such as that in salt marshes dominated by *S. alterniflora*, Delft3D uses the equations proposed by Baptist (2005). In the case of flexible *Z. marina*, Delft3D assumes a greater degree of roughness (Lera *et al*, 2019).

However, models do provide useful insights on the entire bay system suspended sediment distribution. In fact, we can model and measure the mass balance of water flow and sediment distribution, adding multiple sediment characteristics and coupling the hydrodynamic module with Baptist's vegetation model. Baptist's equation has been widely tested with field data and through laboratory experiments with natural and artificial vegetation, as well as with rigid and flexible vegetation. In addition, many experiments have compared the predicted results with experimental data, with comparable outcomes. Baptist (2005) applied his model to the Allier (France), the Volga (Russia), and the Rhine (Netherlands). The results were compared with field data, with the conclusion that the model gave consistent results in terms of the sedimentation differences caused by vegetation. Also, Baptist *et al* (2007) used the results of the depth-averaged kappa–epsilon turbulence model, which accounts for vegetation in a genetic programming framework, to obtain an expression for roughness in the presence of vegetation. Thousands of simulations from this model (using a variety of input parameters) were used as data points for genetic programming to find the dimensionally consistent, symbolic equation for flow roughness due to vegetation. Crosato and Saleh (2011) provide another validation of the Baptist equation on the effects of floodplain vegetation on river planform, with field observations applied to the Allier River in France.

Conclusion

Numerical model results show that bay vegetation reduces sediment export from the VCR into the ocean between summer and winter seasons (Figure 12). In our simulations with fixed bathymetry, we find that ocean waves have a limited impact on bay hydrodynamics. Our study reveals that the ebb dominance of the bay system is not strongly affected by the presence of offshore waves (Figures 6 and 7). However, offshore waves affect tidal inlet hydrodynamics through the alongshore current and sediment dynamics among bays in VCR. Changing the wave angle (ϕ_R) and significant wave height (H_S), our model runs show a variation in velocity at the tidal inlet with values between 1 and 4% compared to the case without waves.

Our results highlight the delicate equilibrium between the effects of bay vegetation and wave climate on the coastal wetlands sediment budget. Our study shows that the alongshore current is strong enough to deliver sediment from one inlet to another, allowing the sediment to re-enter the bay through a different inlet. Additionally, offshore waves increase sediment export from coastal bay systems and play a key role in sediment loss. This study might help administrators and stakeholders to quantify a sediment budget at VCR coastal bays, envisioning possible restoration strategies to reduce sediment export. Our results show an export of sediment from VCR bays under waves attack up to 29%, during summer seasons, while during winter the sediment export might be a few times larger. Further research is needed to quantify and measure coastal bays' sediment budget in the VCR, while approaches such as field

observations of hydrodynamic and sediment transport magnitude are crucial for validating numerical models.

Data Availability Statement

The datasets used and/or analysed during the current study are available from the corresponding author on reasonable request.

Conflict of Interest

The authors declare no conflict of interest.

Acknowledgements—We thank the editors and two anonymous reviewers for suggestions and comments on the manuscript. We would also like to thank Professor Patricia L. Wiberg and Professor Sergio Fagherazzi who provided a fruitful discussion on the initial manuscript idea. This is contribution number 5882 of the University of Maryland Center for Environmental Science – Horn Point Laboratory.

References

Apollone E. 2000. Organic matter distribution and turnover along a gradient from forest to tidal creek. MSc thesis, East Carolina University.

Ashton AD, Giosan L. 2011. Wave-angle control of delta evolution. *Geophysical Research Letters* **38**: L13405. https://doi.org/10.1029/2011GL047630

Aubrey DG, Speer PE. 1984. Updrift migration of tidal inlets. *The Journal of Geology* **92**(5): 531–545.

Baptist M. 2005. Modelling floodplain biogeomorphology. PhD thesis, Delft University of Technology. ISBN 90–407–2582–9.

Baptist MJ, Babovic V, Rodríguez Uthurburu J, Keijzer M, Uittenbogaard RE, Mynett A, Verwey A. 2007. On inducing equations for vegetation resistance. *Journal of Hydraulic Research* **45**(4): 435–450.

Battjes JA, Janssen JPFM. 1978. Energy loss and set-up due to breaking of random waves. *Proc. 16th Int. Conf. Coastal Eng., ASCE*, 569–588.

Boesch DF. 2006. Scientific requirements for ecosystem-based management in the restoration of Chesapeake Bay and Coastal Louisiana. *Ecological Engineering* **26**: 6–26.

Booij N, Ris RC, Holthuijsen LH. 1999. A third-generation wave model for coastal regions, Part I: model description and validation. *Journal of Geophysical Research* **104**: 7649–7666.

Boon JD, III, Byrne RJ. 1981. On basin hypsometry and the morphodynamic response of coastal inlet systems. *Marine Geology* **40**(1–2): 27–48.

Bruun P. 1978. Common reasons for damage or breakdown of mound breakwaters. *Coastal Engineering* **2**: 261–273.

Carr J, D'Odorico P, McGlathery K, Wiberg P. 2010. Stability and bistability of seagrass ecosystems in shallow coastal lagoons: role of feedbacks with sediment resuspension and light attenuation. *Journal of Geophysical Research* **115**: G03011. https://doi.org/10.1029/2009JG001103

Castagno KA, Jiménez-Robles AM, Donnelly JP, Wiberg PL, Fenster MS, Fagherazzi S. 2018. Intense storms increase the stability of tidal bays. *Geophysical Research Letters* **45**: 5491–5500. https://doi.org/10.1029/2018GL078208

Chawla A, Spindler DM, Tolman HL. 2013. Validation of a thirty year wave hindcast using the Climate Forecast System Reanalysis winds. *Ocean Modelling* **70**: 189–206. https://doi.org/10.1016/j.ocemod.2012.07.005

Chauhan, P (2009) Autocyclic erosion in tidal marshes. *Geomorphology*, **110**(3-4), 45–57. https://doi.org/10.1016/j.geomorph.2009.03.016

Cooper S. 1995. Chesapeake Bay watershed historical land use: impact on water quality and diatom communities. *Ecological Applications* **5** (3): 703–723. https://doi.org/10.2307/1941979

Crosato A, Saleh MS. 2011. Numerical study on the effects of floodplain vegetation on river planform style. *Earth Surface Processes and Landforms* **36**: 711–720. https://doi.org/10.1002/esp.2088

Cucco A, Umgiesser G. 2006. Modeling the Venice Lagoon residence time. *Ecological Modelling* **193**: 34–51.

D'Alpaos A, Lanzoni S, Marani M, Rinaldo A. 2007. Landscape evolution in tidal embayments: modeling the interplay of erosion, sedimentation, and vegetation dynamics. *Journal of Geophysical Research: Earth Surface* **112**(F1). https://doi.org/10.1029/2006JF000537.

Duarte CM, Losada IJ, Hendriks IE, Mazarrasa I, Marbà N. 2019. The role of coastal plant communities for climate change mitigation and adaptation. *Nature Climate Change* **3**(11): 961–968. https://doi.org/10.1038/nclimate1970

Escoffier FF. 1977. Hydraulics and Stability of Tidal Inlets. Escoffier (Francis F) Fort Belvoir Va.

Fagherazzi S, Marani M, Blum LK. 2004. *The Ecogeomorphology of Tidal Marshes*. American Geophysical Union: Washington, D.C.

Fagherazzi S, Mariotti G, Wiberg PL, McGlathery KJ. 2013. Marsh collapse does not require sea level rise. *Oceanography* **26**(3): 70–77.

Folmer EO, van der Geest M, Jansen E, Olff H, Anderson TM, Piersma T, van Gils JA. 2012. Seagrass–sediment feedback: an exploration using a non-recursive structural equation model. *Ecosystems* **15**(8): 1380–1393.

Friedrichs CT, Aubrey DG, Giese GS, Speer PE. 1993. Hydrodynamical modeling of a multiple-inlet estuary/barrier system: insight into tidal inlet formation and stabilityModeling, *Coastal and Estuarine Studiesg*, 95.

Fugate DC, Friedrichs CT, Bilgili A. 2006. Estimation of residence time in a shallow back barrier lagoon, Hog Island Bay, Virginia, USA. In *9th International Conference on Estuarine and Coastal Modeling*, Spaulding M (ed.). ASCE: Reston, VA: ASCE Library.

Ganju NK, Nidzieko NJ, Kirwan ML. 2013. Inferring tidal wetland stability from channel sediment fluxes: observations and a conceptual model. *Journal of Geophysical Research: Earth Surface* **118**(4): 2045–2058.

Grant WD, Madsen O. 1979. Combined wave and current interaction with a rough bottom. *Journal of Geophysical Research* **84**(C4): 1979–1808.

Hayes MO. 1979. Barrier island morphology as a function of tidal and wave regime. In *Barrier Islands: From the Gulf of St. Lawrence to the Gulf of Mexico*, Leatherman SP (ed). Academic Press: New York; 1–28.

Hasselmann K, Barnett TP, Bouws E, Carlson H, Cartwright DE, Enke K, Ewing JA, Gienapp H, Hasselmann DE, Kruseman P, Meerburg A, Müller P, Olbers DJ,Richter K,Sell W,Walden H. 1973. Measurements of wind-wave growth and swell decay during the Joint North Sea Wave Project (JONSWAP). Ergänzungzur Deut. Hydrogr. Z., Reihe, **12**(A8): 1–95.

Kemp WM, Boynton WR, Adolf JE, Boesch DF, Boicourt WC, Brush G, Cornwell JC, Fisher TR, Gilbert PM, Hagy JD. 2005. Eutrophication of Chesapeake Bay: historical trends and ecological interactions. *Marine Ecology Progress Series* **303**: 1–29.

Komen G, Hasselmann S, Hasselmann K. 1984. On the existence of a fully developed wind–sea spectrum. *Journal of Physical Oceanography* **14**(8): 1271–1285. https://doi.org/10.1175/1520-0485

Larsen GL, Harvey JW. 2010. How vegetation and sediment transport feedbacks drive landscape change in the everglades and wetlands worldwide. *The American Naturalist* **176**(3): E66–E79.

Lawson SE, Wiberg PL, McGlathery KJ, Fugate DC. 2007. Wind-driven sediment suspension controls light availability in a shallow coastal lagoon. *Estuaries and Coasts* **30**(1): 102–112.

Leonard LA, Luther ME. 1995. Flow hydrodynamics in tidal marsh canopies. *Limnology and Oceanography* **40**(8): 1474–1484.

Lera S, Nardin W, Sanford L, Palinkas C, Guercio R. 2019. The impact of submersed aquatic vegetation on the development of river mouth bars. *Earth Surface Processes and Landforms*, **44**: 1494–1506. https://doi.org/10.1002/esp.4585

Lesser G, Roelvink J, Van Kester J, Stelling G. 2004. Development and validation of a three-dimensional morphological model. *Coastal Engineering* **51**: 883–915.

Loder NM, Irish JL, Cialone MA, Wamsley TV. 2009. Sensitivity of hurricane surge to morphological parameters of coastal wetlands.

Estuarine, Coastal and Shelf Science **84**(4): 625–636. https://doi.org/10.1016/j.ecss.2009.07.036

Marani M, D'Alpaos A, Lanzoni S, Santalucia M. 2011. Understanding and predicting wave erosion of marsh edges. *Geophysical Research Letters* **38**: L21401. https://doi.org/10.1029/2011GL048995

Mariotti G, Fagherazzi S, Wiberg PL, McGlathery KJ, Carniello L, Defina A. 2010. Influence of storm surges and sea level on shallow tidal basin erosive processes. *Journal of Geophysical Research* **115** (C11012). https://doi.org/10.1029/2009JC005892

Mariotti G, Fagherazzi S. 2013. Critical width of tidal flats triggers marsh collapse in the absence of sea-level rise. *Proceedings of the National Academy of Sciences* **110**: 5353–5356. https://doi.org/10.1073/pnas.1219600110

Mariotti G, Canestrelli A. 2017. Long-term morphodynamics of muddy backbarrier basins: fill in or empty out? *Water Resources Research* **53**: 7029–7054. https://doi.org/10.1002/2017WR020461

McGlathery KJ, Anderson IC, Tyler AC. 2001. Magnitude and variability of benthic and pelagic metabolism in a temperate coastal lagoon. *Marine Ecology Progress Series* **216**: 1–15.

McGlathery KJ, Sundback K, Anderson IC. 2007. Eutrophication patterns in shallow coastal bays and lagoons: the role of plants in the coastal filter. *Marine Ecology Progress Series* **348**: 1–18.

McLoughlin SM, Wiberg PL, Safak I, McGlathery KJ. 2015. Rates and forcing of marsh edge erosion in a shallow coastal bay. *Estuaries and Coasts* **38**: 620–638. https://doi.org/10.1007/s12237-014-9841-2

Moeller I, Spencer T, French JR. 1996. Wave attenuation over saltmarsh surfaces: preliminary results from Norfolk, England. *Journal of Coastal Research* **12**(4): 1009–1016.

Möller I, Kudella M, Rupprecht F, Spencer T, Paul M, van Wesenbeeck BK, Wolters G, Jensen K, Bouma TJ, Miranda-Lange M, Schimmels S. 2014. Wave attenuation over coastal salt marshes under storm surge conditions. *Nature Geoscience* **7**: 727–731. https://doi.org/10.1038/ngeo2251

Moore KA. 2004. Influence of seagrasses on water quality in shallow regions of the lower Chesapeake Bay. *Journal of Coastal Research* **45**: 162–178.

Nardin W, Edmonds DA. 2014. Optimum vegetation height and density for inorganic sedimentation in deltaic marshes. *Nature Geoscience* **7** (10): 722–726. https://doi.org/10.1038/ngeo2233

Nardin W, Edmonds DA, Fagherazzi S. 2016. Influence of vegetation on spatial patterns of sediment deposition in deltaic islands during flood. *Advances in Water Resources*, **93**: 236–248. https://doi.org/10.1016/j.advwatres.2016.01.001

Nardin W, Larsen L, Fagherazzi S, Wiberg P. 2018. Tradeoffs among hydrodynamics, sediment fluxes and vegetation community in the Virginia Coast Reserve, USA. *Estuarine, Coastal and Shelf Science* **210**: 98–108. https://doi.org/10.1016/j.ecss.2018.06.009

Nepf HM. 1999. Drag, turbulence, and diffusion in flow through emergent vegetation. *Water Resources Research* **35**(2): 479–489.

Newell RI, Koch EW. 2004. Modeling seagrass density and distribution in response to changes in turbidity stemming from bivalve filtration and seagrass sediment stabilization. *Estuaries* **27**(5): 793–806.

Nichols MM, Boon JD. 1994. Sediment transport processes in coastal lagoons. In *Coastal Lagoon Processes*, Kjerfve B (ed). Elsevier, Amsterdam; 157–219.

Nienhuis JH, Ashton AD. 2016. Mechanics and rates of tidal inlet migration: modeling and application to natural examples. *Journal of Geophysical Research: Earth Surface* **121**(11): 2118–2139. https://doi.org/10.1002/2016JF004035

Nienhuis J, Lorenzo-Trueba J. 2019. Can barrier islands survive sea-level rise? Quantifying the relative role of tidal deltas and overwash deposition. *Geophysical Research Letters* **46**(14): 613–621 https://agupubs.onlinelibrary.wiley.com/doi/full/10.1029/2019GL085524

O'Brien MP. 1969. Equilibrium flow areas of inlets on sandy coasts. *Journal of the Waterways and Harbors Coastal Engineering Division, ASCE* **95**: 43–55.

Oertel GF, Carlson C, Overman K. 2000. Bathymetry of Hog Island Bay, Virginia Coast Reserve Long-Term Ecological Research Project. Data Publication knblter-vcr.143.12.

Oertel GF. 2001. Hypsographic, hydro-hypsographic and hydrological analysis of coastal bay environments, Great Machipongo Bay, Virginia. *Journal of Coastal Research* **17**(4): 775–783.

Partheniades E. (1965). Erosion and deposition of cohesive soils: American Society of Civil Engineers. *Journal of the Hydraulics Division, ASCE*, **92**(1): 79–81.

Reynolds LK, Waycott M, McGlathery KJ, Orth RJ, Zieman JC. 2012. Eelgrass restoration by seed maintains genetic diversity: case study from a coastal bay system. *Marine Ecology Progress Series* **448**: 223–233.

Richardson D, Porter J, Oertel G, Zimmerman R, Carlson C, Overman K. 2014. Integrated topography and bathymetry for the eastern shore of Virginia. Long Term Ecological Research Network. https://doi.org/10.6073/pasta/beb98b208602e0d137acd8497edc3c2d

Safak I, Wiberg PL. 2012. Hydrodynamics and wave-enhanced sediment transport in a barrier island–lagoon–marsh system: a model application on the eastern shore of Virginia. Abstract 029-9350. Presented at *2012 Ocean Sciences Meeting*, American Geophysical Union, Salt Lake City, UT.

Safak I, Wiberg PL, Richardson DL, Kurum MO. 2015. Controls on residence time and exchange in a system of shallow coastal bays. *Continental Shelf Research* **97**(1): 7–20.

Soulsby RL, Davies AG, Fredsoe J, Huntley DA, Jonnson IG, Myrhaug D, Simons RR, Temperville A, Zitman TJ. 1993. Bed shear stresses due to combined waves and currents. In *Abstracts-in-Depth of the Marine Science and Technology G8-M Overall Workshop, Grenoble*; 246.

Stive MJF, Wang ZB, Capobianco M, Ruol P, Buijsman MC. 1998. Morphodynamics of a tidal lagoon and the adjacent coast. In *Physics of Estuaries and Coastal Seas*, Dronkers J, Scheffers MBAM (eds). Balkema: Rotterdam; 397–407.

Temmerman S, Bouma TJ, Govers G, Wang ZB, De Vries MB, Herman PMJ. 2005. Impact of vegetation on flow routing and sedimentation patterns: three-dimensional modeling for a tidal marsh. *Journal of Geophysical Research: Earth Surface* **110**(F4).

Temmerman S, Meire P, Bouma TJ, Herman PMJ, Ysebaert T, De Vriend HJ. 2013. Ecosystem-based coastal defence in the face of global change. *Nature* **504**(7478): 79–83. https://doi.org/10.1038/nature12859

Van de Kreeke J. 1990. Can multiple tidal inlets be stable? *Estuarine, Coastal and Shelf Science* **30**(3): 261–273.

van Rijn LC. 1993. *Principles of Sediment Transport in Rivers, Estuaries, and Coastal Seas*. Aqua Publications: Amsterdam.

Walters D, Moore LJ, Vinent OD, Fagherazzi S, Mariotti G. 2014. Interactions between barrier islands and backbarrier marshes affect island system response to sea level rise: insights from a coupled model. *Journal of Geophysical Research, Series F* **119**: 1–19.

Wiberg PL, Carr JA, Safak I, Anutaliya A. 2015. Quantifying the distribution and influence of non-uniform bed properties in shallow coastal bays. *Limnology and Oceanography: Methods* **13**: 746–762. https://doi.org/10.1002/lom3.10063